Improving the MITC3 shell finite element by using the Hellinger–Reissner principle

Youngyu Lee, Kyungho Yoon, Phill-Seung Lee *

Division of Ocean Systems Engineering, Korea Advanced Institute of Science and Technology, 291 Daehak-ro, Yuseong-gu, Daejeon 305-701, Republic of Korea

ABSTRACT

The objective of this study is to improve the performance of the MITC3 shell finite element. The Hellinger–Reissner (HR) variational principle is modified in the framework of the MITC method, and a special approximated transverse shear strain field is proposed. The MITC3-HR shell finite element improved by using the Hellinger–Reissner functional passes all the basic tests (zero energy mode test, patch test, and isotropic element test). Convergence studies considering a fully clamped plate problem, a sixty-degree skew plate problem, cylindrical shell problems, and hyperboloid shell problems demonstrate the improved predictive capability of the new 3-node shell finite element.

© 2012 Elsevier Ltd. All rights reserved.

1. Introduction

Shell structures have been widely used in many engineering applications, and the finite element method has been dominantly adopted for the analysis of shells. Since the effectiveness of a shell finite element analysis depends highly on the predictive capability of shell finite elements, there is strong demand for the development of more effective shell finite elements [1–3].

The kinematical behavior of shells is very complicated, especially as the shell thickness becomes smaller. Depending on shell geometries, boundary conditions, and applied loadings, the asymptotic behavior can be dominated by membrane or bending actions or a combination of both actions [3–10]. A reliable shell finite element should provide accurate solutions irrespective of the complicated asymptotic behaviors and the magnitude of the shell thickness. However, it is extremely challenging to develop such shell finite elements due to a locking phenomenon; that is, the shell finite element becomes too stiff when the thickness is relatively small in bending situations [1,11].

The MITC (Mixed Interpolation of Tensorial Components) method has been successfully used to develop shell finite elements to reduce the locking effects [12–17]. The MITC4 quadrilateral shell finite elements were first developed by Dvorkin and Bathe [12,13]. The MITC9 and MITC16 quadrilateral shell finite elements were later developed by Bucalem and Bathe [14]. In spite of the fact that triangular elements are very useful for the mesh generation of arbitrary shell geometries, due to the relatively complicated representation of triangular geometries in the element formulation, the MITC method was recently applied to develop isotropic triangular shell elements, MITC3 and MITC6, by Lee and Bathe [15].

The MITC3 triangular shell finite element shows much better predictive capability than the displacement-based 3-node triangular shell finite elements and other 3-node isotropic triangular shell finite elements [15,18]. However, the locking alleviation by MITC3 is not as large as that by MITC4; that is, the accuracy of the solutions is not as good as that of the MITC4 quadrilateral shell finite elements due to locking. This provided the motivation for this work.

The purpose of this paper is to improve the MITC3 shell finite element. With the help of the Hellinger–Reissner (HR) principle [1], we additionally approximate the transverse shear strain fields of the MITC3 shell finite element. The Hellinger–Reissner (HR) functional has been used to alleviate locking in plate and shell finite elements [19,20]. The successful use of this method depends on how the approximated transverse shear strain fields are constructed. We first modify the Hellinger–Reissner functional and introduce a special approximated transverse shear strain field based on rotated contravariant bases.

In the following sections, the MITC3 formulation is briefly reviewed and the Hellinger–Reissner principle for the shell finite element is presented. We then propose a method that involves the use of the Hellinger–Reissner functional to improve the MITC3 shell finite element, after which we explain how to construct the special approximated transverse shear strain field. The basic test results and well-established convergence studies numerically show that the MITC3 shell finite element is successfully improved.

2. Formulation of the MITC3 shell finite element

The geometry of a 3-node continuum mechanics based triangular shell finite element is interpolated by Lee and Bathe [15] and Lee et al. [18]

$$\vec{x}(r,s,t) = \sum_{i=1}^{3} h_i(r,s)\vec{x}_i + \frac{t}{2}\sum_{i=1}^{3} a_i h_i(r,s)\vec{V}_n^i, \tag{1}$$

where $h_i(r,s)$ is the 2D shape function of the standard isoparametric procedure corresponding to node i, $\vec{x}_i$ is the position vector for node i in the global Cartesian coordinate system, and a_i and $\vec{V}_n^i$ denote the shell thickness and the director vector at node i, respectively; see Fig. 1.

The displacement interpolation of the element is obtained by

$$\vec{u}(r,s,t) = \sum_{i=1}^{3} h_i(r,s)\vec{u}_i + \frac{t}{2}\sum_{i=1}^{3} a_i h_i(r,s)(-\vec{V}_2^i\alpha_i + \vec{V}_1^i\beta_i), \tag{2}$$

in which $\vec{u}_i$ is the nodal displacement vector in the global Cartesian coordinate system, $\vec{V}_1^i$ and $\vec{V}_2^i$ are unit vectors orthogonal to $\vec{V}_n^i$ and to each other, and α_i and β_i are the rotations of the director vector $\vec{V}_n^i$ about $\vec{V}_1^i$ and $\vec{V}_2^i$ at node i.

The linear terms of the displacement-based covariant strain components are given by

$$e_{ij} = \frac{1}{2}(\vec{g}_i \cdot \vec{u}_{,j} + \vec{g}_j \cdot \vec{u}_{,i}), \tag{3}$$

where

$$\vec{g}_i = \frac{\partial \vec{x}}{\partial r_i}, \quad \vec{u}_{,i} = \frac{\partial \vec{u}}{\partial r_i} \qquad \text{with } r_1 = r,\ r_2 = s,\ r_3 = t. \tag{4}$$

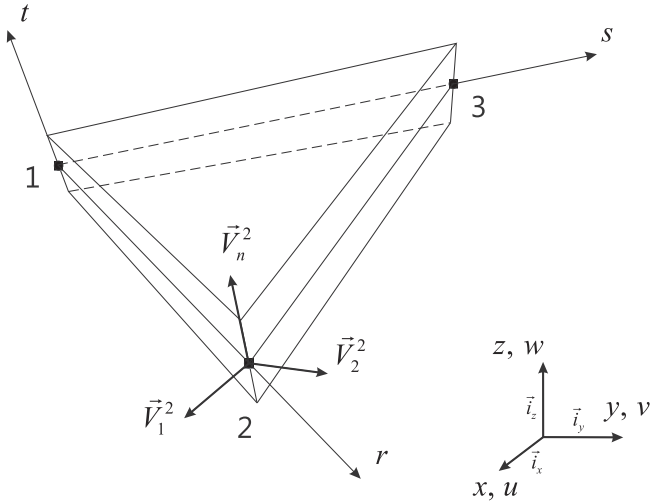**Fig. 1.** A 3-node triangular continuum mechanics based shell finite element.

The covariant strain components can be expressed by

$$e_{ij} = \boldsymbol{b}_{ij}\vec{U}, \tag{5}$$

in which $\boldsymbol{b}_{ij}$ is the covariant strain–displacement matrix and $\vec{U}$ is the vector of nodal displacements and rotations, which include $\vec{u}_k$, α_k, and β_k.

The base vectors of the shell-aligned local Cartesian coordinate system are defined as follows

$$\vec{L}_{\bar{t}} = \frac{\vec{g}_t}{|\vec{g}_t|}, \quad \vec{L}_{\bar{r}} = \frac{\vec{g}_s \times \vec{L}_{\bar{t}}}{|\vec{g}_s \times \vec{L}_{\bar{t}}|}, \quad \vec{L}_{\bar{s}} = \vec{L}_{\bar{t}} \times \vec{L}_{\bar{r}}. \tag{6}$$

The strains (ε_{ij}) defined in the shell-aligned local Cartesian coordinate are calculated from the covariant strain components through the following relation,

$$\varepsilon_{ij}(\vec{L}_i \otimes \vec{L}_j) = e_{mn}(\vec{g}^m \otimes \vec{g}^n) \quad \text{with } \vec{L}_1 = \vec{L}_{\bar{r}},\ \vec{L}_2 = \vec{L}_{\bar{s}},\ \vec{L}_3 = \vec{L}_{\bar{t}}. \tag{7}$$

In Eq. (7), the contravariant base vectors $\vec{g}^j$ are given by

$$\vec{g}_i \cdot \vec{g}^j = \delta_i^j \quad \text{with } \vec{g}^1 = \vec{g}^r,\ \vec{g}^2 = \vec{g}^s,\ \vec{g}^3 = \vec{g}^t, \tag{8}$$

where δ_i^j is the Kronecker delta in mixed form.

The strain vector defined in the shell-aligned local Cartesian coordinate system from the displacement-based shell formulation is

$$\vec{\varepsilon} = \boldsymbol{B}\vec{U}, \tag{9}$$

where $\vec{\varepsilon} = [\,\varepsilon_{\bar{r}\bar{r}} \quad \varepsilon_{\bar{s}\bar{s}} \quad 2\varepsilon_{\bar{r}\bar{s}} \quad 2\varepsilon_{\bar{s}\bar{t}} \quad 2\varepsilon_{\bar{r}\bar{t}}\,]^T$.

In the formulation of the MITC3 shell finite element, the covariant in-plane strain field is calculated by the displacement-based triangular shell formulation in Eq. (3) and the MITC method is only applied to substitute the covariant transverse shear strain field [15]. The assumed covariant transverse shear strain components, which are spatially isotropic, are given by

$$\tilde{e}_{rt} = e_{rt}^{(1)} + cs, \quad \tilde{e}_{st} = e_{st}^{(2)} - cr, \tag{10}$$

where $c = e_{st}^{(2)} - e_{rt}^{(1)} - e_{st}^{(3)} + e_{rt}^{(3)}$ and, at the tying points, $e_{rt}^{(n)}$ and $e_{st}^{(n)}$ are calculated from Eq. (3), see Fig. 2.

The assumed covariant transverse shear strain components of the MITC3 element can also be expressed by

$$\tilde{e}_{ij} = \tilde{\boldsymbol{b}}_{ij}\vec{U}. \tag{11}$$

The covariant strains of the MITC3 shell finite element are transformed to the strains defined in the shell-aligned local Cartesian coordinate system ($\vec{L}_{\bar{r}}, \vec{L}_{\bar{s}}, \vec{L}_{\bar{t}}$)

$$\vec{\varepsilon}^M = \boldsymbol{B}^M\vec{U} \quad \text{with } \vec{\varepsilon}^M = [\,\varepsilon_{\bar{r}\bar{r}}^M \quad \varepsilon_{\bar{s}\bar{s}}^M \quad 2\varepsilon_{\bar{r}\bar{s}}^M \quad 2\varepsilon_{\bar{s}\bar{t}}^M \quad 2\varepsilon_{\bar{r}\bar{t}}^M\,]^T. \tag{12}$$
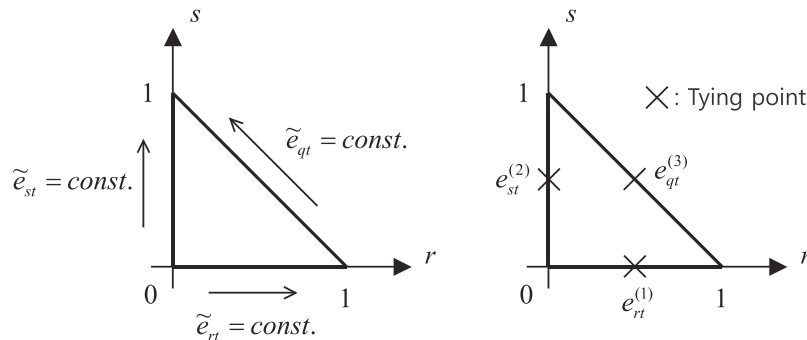

Fig. 2. Tying positions for the transverse shear strain of the MITC3 triangular shell finite element. The constant transverse shear strain condition is imposed along its edges.

3. The Hellinger–Reissner principle for 3-node shell finite elements

The Hellinger–Reissner functional (HR functional), which is derived from the Hu–Washizu functional [1], is given by

$$\Pi_{HR} = \int_V \left(-\frac{1}{2}\vec{\varepsilon}^T \mathbf{C}\vec{\varepsilon} + \vec{\varepsilon}^T \mathbf{C}\partial_\varepsilon \vec{u} \right) dV - \int_V \vec{u}^T \vec{f}^B \, dV - \int_{S_f} \vec{u}^{S_f^T} \vec{f}^{S_f} \, dS$$
$$- \int_{S_u} \vec{f}^{S_u^T} (\vec{u}^{S_u} - \vec{u}_p) \, dS, \tag{13}$$

where $\vec{\varepsilon}$ is the strain vector, $\mathbf{C}$ is the stress–strain law matrix, $\vec{u}$ is the displacement vector, ∂_ε is the differential operator on $\vec{u}$ for strain calculations, $\vec{f}^B$ is the vector for body forces, $\vec{f}^{S_f}$ is the vector for applied surface tractions, $\vec{u}_p$ is the vector for prescribed displacements, V is the volume of the body, S_f is the surface on which $\vec{f}^{S_f}$ is applied, S_u is the surface on which $\vec{u}_p$ is prescribed, $\vec{u}^{S_f}$ is the displacement vector over S_f, $\vec{u}^{S_u}$ is the displacement vector over S_u, and $\vec{f}^{S_u}$ is the reaction vector calculated by the stresses on S_u. It is important to note that the independent variables are strains and displacements in this Hellinger–Reissner functional.

For the 3-node shell finite element formulation, the Hellinger–Reissner functional is changed to separate the bending and membrane strains and the transverse shear strains as follows

$$\Pi_{HR}^S = \int_V \left(\frac{1}{2}\vec{\varepsilon}_{bm}^T \mathbf{C}_{bm}\vec{\varepsilon}_{bm} - \frac{1}{2}\vec{\gamma}^{A^T} \mathbf{C}_\gamma \vec{\gamma}^A + \vec{\gamma}^{A^T} \mathbf{C}_\gamma \vec{\gamma} \right) dV$$
$$- \int_V \vec{u}^T \vec{f}^B \, dV - \int_{S_f} \vec{u}^{S_f^T} \vec{f}^{S_f} \, dS - \int_{S_u} \vec{f}^{S_u^T} (\vec{u}^{S_u} - \vec{u}_p) \, dS, \tag{14}$$

where $\vec{\varepsilon}_{bm}$ is the vector for the displacement-based bending and membrane strains, $\vec{\gamma}$ is the vector for the displacement-based transverse shear strains, and $\vec{\gamma}^A$ is the vector for the approximated transverse shear strains with unknowns,

$$\vec{\varepsilon}_{bm} = \begin{pmatrix} \varepsilon_{\bar{r}\bar{r}} \\ \varepsilon_{\bar{s}\bar{s}} \\ 2\varepsilon_{\bar{r}\bar{s}} \end{pmatrix}, \quad \vec{\gamma} = \begin{pmatrix} 2\varepsilon_{\bar{s}\bar{t}} \\ 2\varepsilon_{\bar{r}\bar{t}} \end{pmatrix}, \quad \vec{\gamma}^A = \begin{pmatrix} 2\varepsilon_{\bar{s}\bar{t}}^A \\ 2\varepsilon_{\bar{r}\bar{t}}^A \end{pmatrix}, \tag{15}$$

and all the strain components are defined in the shell-aligned local Cartesian coordinate system to satisfy the material stress–strain law for shells.

In Eq. (14), $\mathbf{C}_{bm}$ is the stress–strain law matrix for the bending and membrane strains and $\mathbf{C}_\gamma$ is the stress–strain law matrix for the transverse shear strains,

$$\mathbf{C}_{bm} = \frac{E}{1-v^2} \begin{bmatrix} 1 & v & 0 \\ v & 1 & 0 \\ 0 & 0 & \frac{1-v}{2} \end{bmatrix}, \quad \mathbf{C}_\gamma = \frac{E}{1-v^2} \begin{bmatrix} k\frac{1-v}{2} & 0 \\ 0 & k\frac{1-v}{2} \end{bmatrix}, \tag{16}$$

where E, v, and k are Young' modulus, Poisson's ratio, and a shear correction factor, respectively. In this work, we use $k = 1.0$.

In general, $\vec{\varepsilon}_{bm}$ and $\vec{\gamma}$ come from the 3-node displacement-based shell formulation; that is, $\vec{\varepsilon}_{bm}$ and $\vec{\gamma}$ are obtained by Eq. (9)

$$\vec{\varepsilon}_{bm} = \begin{pmatrix} \varepsilon_{\bar{r}\bar{r}} \\ \varepsilon_{\bar{s}\bar{s}} \\ 2\varepsilon_{\bar{r}\bar{s}} \end{pmatrix} = \mathbf{B}_{bm}\vec{U}, \quad \vec{\gamma} = \begin{pmatrix} 2\varepsilon_{\bar{s}\bar{t}} \\ 2\varepsilon_{\bar{r}\bar{t}} \end{pmatrix} = \mathbf{B}_\gamma \vec{U}. \tag{17}$$

The approximated transverse shear strain field ($\vec{\gamma}^A$) is constructed with the appropriate interpolation with unknowns ($\vec{\alpha}$),

$$\vec{\gamma}^A = \begin{pmatrix} 2\varepsilon_{\bar{s}\bar{t}}^A \\ 2\varepsilon_{\bar{r}\bar{t}}^A \end{pmatrix} = \mathbf{B}_\gamma^A \vec{\alpha}. \tag{18}$$

Finally, the unknown variables in Eq. (14) are the nodal displacements and rotations ($\vec{U}$) and the approximated transverse shear strains ($\vec{\alpha}$). The effectiveness of the shell finite element formulation

based on the Hellinger–Reissner principle highly depends on how the interpolation function is constructed in Eq. (18).

4. Formulation of the MITC3-HR shell finite element

We here modify the Hellinger–Reissner functional in Eq. (14) as follows

$$\Pi_{HR}^M = \int_V \left(\frac{1}{2}\vec{\varepsilon}_{bm}^{M^T} \mathbf{C}_{bm}\vec{\varepsilon}_{bm}^M - \frac{1}{2}\vec{\gamma}^{A^T} \mathbf{C}_\gamma \vec{\gamma}^A + \vec{\gamma}^{A^T} \mathbf{C}_\gamma \vec{\gamma}^M \right) dV$$
$$- \int_V \vec{u}^T \vec{f}^B \, dV - \int_{S_f} \vec{u}^{S_f^T} \vec{f}^{S_f} \, dS - \int_{S_u} \vec{f}^{S_u^T} (\vec{u}^{S_u} - \vec{u}_p) \, dS \tag{19}$$

with

$$\vec{\varepsilon}_{bm}^M = \begin{pmatrix} \varepsilon_{\bar{r}\bar{r}}^M \\ \varepsilon_{\bar{s}\bar{s}}^M \\ 2\varepsilon_{\bar{r}\bar{s}}^M \end{pmatrix} = \mathbf{B}_{bm}^M \vec{U}, \quad \vec{\gamma}^M = \begin{pmatrix} 2\varepsilon_{\bar{s}\bar{t}}^M \\ 2\varepsilon_{\bar{r}\bar{t}}^M \end{pmatrix} = \mathbf{B}_\gamma^M \vec{U}, \quad \vec{\gamma}^A = \begin{pmatrix} 2\varepsilon_{\bar{s}\bar{t}}^A \\ 2\varepsilon_{\bar{r}\bar{t}}^A \end{pmatrix} = \mathbf{B}_\gamma^A \vec{\alpha}, \tag{20}$$

in which $\vec{\varepsilon}_{bm}^M$ and $\vec{\gamma}^M$ are the vector for the bending and membrane strains and the vector for the transverse shear strains obtained by Eq. (12) in the MITC3 shell finite element formulation.

This is a very important modification of the Hellinger–Reissner functional. As a result, the new element, MITC3-HR, is based on the formulation of the MITC3 shell finite element. It provides strong potential to improve the MITC3 shell finite element. Since the MITC formulation can be represented by the Hellinger–Reissner principle [21], the Hellinger–Reissner principle is, in effect, used twice in our formulation.

Another important part for successful development is the approach taken to construct the approximated transverse strain field, which should retain the isotropic property as well as improve the predictive capability of the MITC3 shell finite element. For the construction of $\vec{\gamma}^A$ in Eq. (20), we use a special approximated transverse shear strain field introduced on the rotated contravariant base vectors. The components of $\vec{\gamma}^A$ are given by

$$2\varepsilon_{\bar{r}\bar{t}}^A = 2\tilde{e}_{st}^A [(\vec{g}^{s'} \cdot \overrightarrow{L}_{\bar{r}})(\vec{g}^{t'} \cdot \overrightarrow{L}_{\bar{t}}) + (\vec{g}^{t'} \cdot \overrightarrow{L}_{\bar{r}})(\vec{g}^{s'} \cdot \overrightarrow{L}_{\bar{t}})]$$
$$+ 2\tilde{e}_{rt}^A [(\vec{g}^{r'} \cdot \overrightarrow{L}_{\bar{r}})(\vec{g}^{t'} \cdot \overrightarrow{L}_{\bar{t}}) + (\vec{g}^{t'} \cdot \overrightarrow{L}_{\bar{r}})(\vec{g}^{r'} \cdot \overrightarrow{L}_{\bar{t}})],$$
$$2\varepsilon_{\bar{s}\bar{t}}^A = 2\tilde{e}_{st}^A [(\vec{g}^{s'} \cdot \overrightarrow{L}_{\bar{s}})(\vec{g}^{t'} \cdot \overrightarrow{L}_{\bar{t}}) + (\vec{g}^{t'} \cdot \overrightarrow{L}_{\bar{s}})(\vec{g}^{s'} \cdot \overrightarrow{L}_{\bar{t}})]$$
$$+ 2\tilde{e}_{rt}^A [(\vec{g}^{r'} \cdot \overrightarrow{L}_{\bar{s}})(\vec{g}^{t'} \cdot \overrightarrow{L}_{\bar{t}}) + (\vec{g}^{t'} \cdot \overrightarrow{L}_{\bar{s}})(\vec{g}^{r'} \cdot \overrightarrow{L}_{\bar{t}})] \tag{21}$$

with

$$\tilde{e}_{rt}^A = \alpha_2 + \alpha_3 s, \quad \tilde{e}_{st}^A = \alpha_1 - \alpha_3 r, \tag{22}$$

in which $\vec{g}^{r'}$, $\vec{g}^{s'}$, and $\vec{g}^{t'}$ are the rotated contravariant base vectors and α_1, α_2, and α_3 are the unknown variables for the approximated covariant transverse shear strains. Here, it is important to note that the type of interpolation functions in Eq. (22) is the same as that of the interpolation functions used in Eq. (10), which belong to a "rotated Raviart–Thomas space".

In order to calculate the rotated contravariant base vectors, as shown in Fig. 3, we first rotate the three covariant base vectors about the vector ($\vec{e}_n$) normal to the midsurface ($t = 0$) of the shell element

$$\vec{g}_i' = \cos\theta\vec{g}_i + (1 - \cos\theta)(\vec{g}_i \cdot \vec{e}_n)\vec{e}_n + (\vec{e}_n \times \vec{g}_i)\sin\theta \tag{23}$$

with

$$\vec{e}_n = \frac{\vec{g}_r \times \vec{g}_s}{|\vec{g}_r \times \vec{g}_s|}, \tag{24}$$

in which $\vec{g}_i$ are the covariant base vectors ($i = r$, s, and t) evaluated by Eq. (4) at the integration points of the shell element, and θ is the angle of rotation about $\vec{e}_n$. The rotated contravariant base vectors are then calculated by
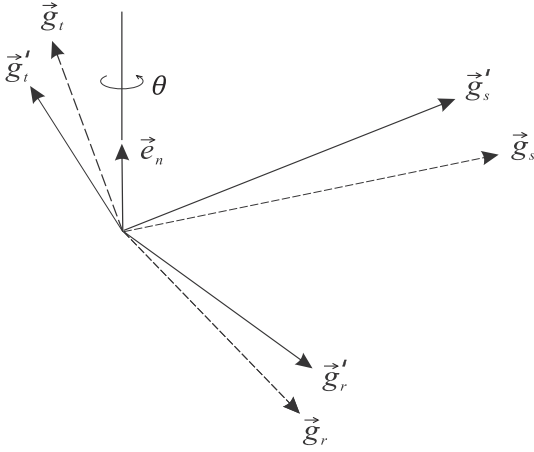
Fig. 3. The rotated covariant base vectors for the MITC3-HR shell finite element. The dotted and solid vectors correspond to the original and rotated covariant base vectors, respectively.

$$\vec{g}_i' \cdot \vec{g}^{j'} = \delta_i^j. \tag{25}$$

Note that $\vec{e}_n$ is a constant vector, because the midsurface of the 3-node shell element is flat.

Invoking $\delta\Pi_{HR}^M = 0$ in Eq. (19), we obtain

$$\begin{bmatrix} \boldsymbol{K}_{uu} & \boldsymbol{K}_{u\varepsilon} \\ \boldsymbol{K}_{\varepsilon u} & \boldsymbol{K}_{\varepsilon\varepsilon} \end{bmatrix} \begin{pmatrix} \vec{U} \\ \vec{\alpha} \end{pmatrix} = \begin{pmatrix} \vec{R} \\ \vec{0} \end{pmatrix} \tag{26}$$

and, using the static condensation on $\vec{\alpha}$, the stiffness matrix of the MITC3-HR shell finite element is finally given as

$$\boldsymbol{K} = \boldsymbol{K}_{uu} - \boldsymbol{K}_{u\varepsilon}\boldsymbol{K}_{\varepsilon\varepsilon}^{-1}\boldsymbol{K}_{u\varepsilon}^T \tag{27}$$

with

$$\boldsymbol{K}_{uu} = \int_V \boldsymbol{B}_{bm}^{M^T}\boldsymbol{C}_{bm}\boldsymbol{B}_{bm}^M \, dV,$$

$$\boldsymbol{K}_{u\varepsilon} = \int_V \boldsymbol{B}_{\gamma}^{M^T}\boldsymbol{C}_{\gamma}\boldsymbol{B}_{\gamma}^A \, dV,$$

$$\boldsymbol{K}_{\varepsilon\varepsilon} = -\int_V \boldsymbol{B}_{\gamma}^{A^T}\boldsymbol{C}_{\gamma}\boldsymbol{B}_{\gamma}^A \, dV. \tag{28}$$

After obtaining the nodal displacement solution $\vec{U}$, $\vec{\alpha}$ is given by

$$\vec{\alpha} = -\boldsymbol{K}_{\varepsilon\varepsilon}^{-1}\boldsymbol{K}_{u\varepsilon}^T\vec{U}, \tag{29}$$

and the strains are then calculated by $\vec{\varepsilon}_{bm}^M$ and $\tilde{\gamma}^A$ in Eq. (20), and the stresses are obtained using the stress–strain law in Eq. (16).

5. Basic numerical tests

In this section, the results of three basic tests of the MITC3-HR shell finite elements are presented.

5.1. Strain energy mode test

We count how many zero eigenvalues exist in the stiffness matrix of a single unsupported element. The single shell finite element should pose exactly six zero eigenvalues, corresponding to the six physical rigid body modes. When a shell finite element has additional zero eigenvalues corresponding to spurious energy modes, the stability of the solutions cannot be guaranteed. This test is called the zero energy mode test. The MITC3-HR shell finite element passes the zero energy mode test except for the case where the angle θ in Eq. (23) is 90 deg and the element has a uniform thickness.

Tables 1 and 2 present the eigenvalues of the strain energy modes of the MITC3-HR shell finite element according to the rotation angle (θ) of the contravariant base vector for the plate bending problem shown in Fig. 4(a) when t/L is 0.001 and 0.0001 (uniform thickness). Because the eigenvalues change with the order of $(t/L)^3$ in the modes 7, 8, and 9, these modes are easily identified as bending modes. After investigating the strain distributions by the modes 11 and 13, it is found that these two modes include both transverse shear and bending modes.

When the angle $\theta = 0$, all of the eigenvalues of the MITC3-HR shell finite element are identical to those of the MITC3 shell finite element. As the angle θ increases to 90 deg, the 10th eigenvalue decreases. Fig. 5 presents the 10th mode shapes ($\theta = 89$ deg) of the displacement based 3-node, MITC3 and MITC3-HR shell finite elements. It is very interesting to note that, while the 10th strain energy mode of the displacement based 3-node shell element is the pure in-plane twisting mode (Fig. 5(a)), the 10th modes of MITC3
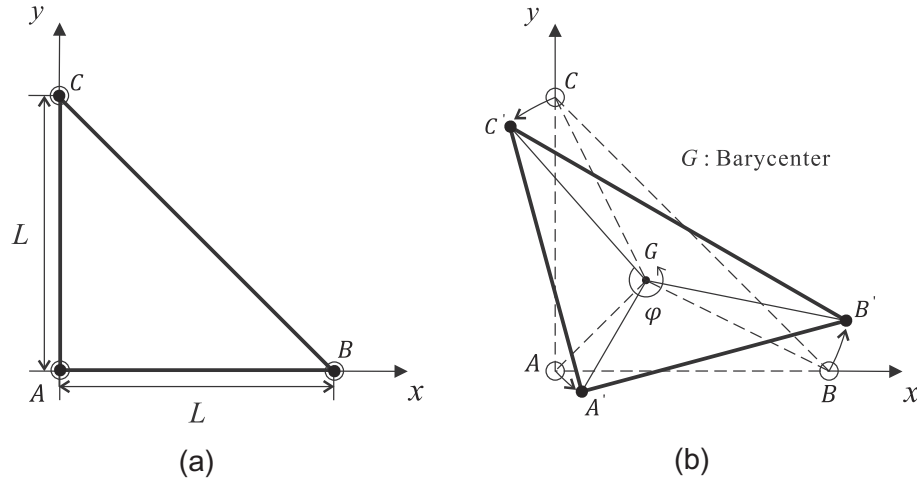
Table 1
The eigenvalues of the strain energy modes of the MITC3-HR shell finite element for the plate bending problem shown in Fig. 4(a) when t/L = 0.001. Modes 1–6 are rigid body modes. Modes 12, 14 and 15 are membrane modes.

Mode	Angle (θ)				
	0 deg (MITC3)	30 deg	60 deg	89 deg	90 deg
7	6.6764E−04	6.6764E−04	6.6764E−04	6.6764E−04	6.6764E−04
8	8.1454E−04	8.1454E−04	8.1454E−04	8.1265E−04	1.0752E−03
9	2.4924E−03	2.4924E−03	2.4924E−03	2.4924E−03	2.4924E−03
10	3.6928E+02	2.7702E+02	9.2381E+01	1.1284E−01	0.0000E+00
11	4.6707E+03	4.6696E+03	4.6676E+03	4.6667E+03	4.6667E+03
13	1.1760E+04	1.1760E+04	1.1760E+04	1.1760E+04	1.1760E+04

Table 2
The eigenvalues of the strain energy modes of the MITC3-HR shell finite element for the plate bending problem shown in Fig. 4(a) when t/L = 0.0001. Modes 1–6 are rigid body modes. Modes 12, 14 and 15 are membrane modes.

Mode	Angle (θ)				
	0 deg (MITC3)	30 deg	60 deg	89 deg	90 deg
7	6.6764E−07	6.6764E−07	6.6764E−07	6.6764E−07	6.6764E−07
8	8.1455E−07	8.1455E−07	8.1455E−07	8.1453E−07	1.0752E−06
9	2.4924E−06	2.4924E−06	2.4924E−06	2.4924E−06	2.4924E−06
10	3.6928E+01	2.7702E+01	9.2381E+00	1.1258E−02	0.0000E+00
11	4.6707E+02	4.6696E+02	4.6676E+02	4.6667E+02	4.6667E+02
13	1.1760E+03	1.1760E+03	1.1760E+03	1.1760E+03	1.1760E+03

Fig. 4. Strain energy mode test ($L = 1.0$, $E = 1.7472 \times 10^7$ and $v = 0.3$). (a) A single triangular shell finite element. (b) In-plane twisting mode for the single shell finite element. The dotted and solid lines correspond to the top surfaces before and after deformation, respectively.
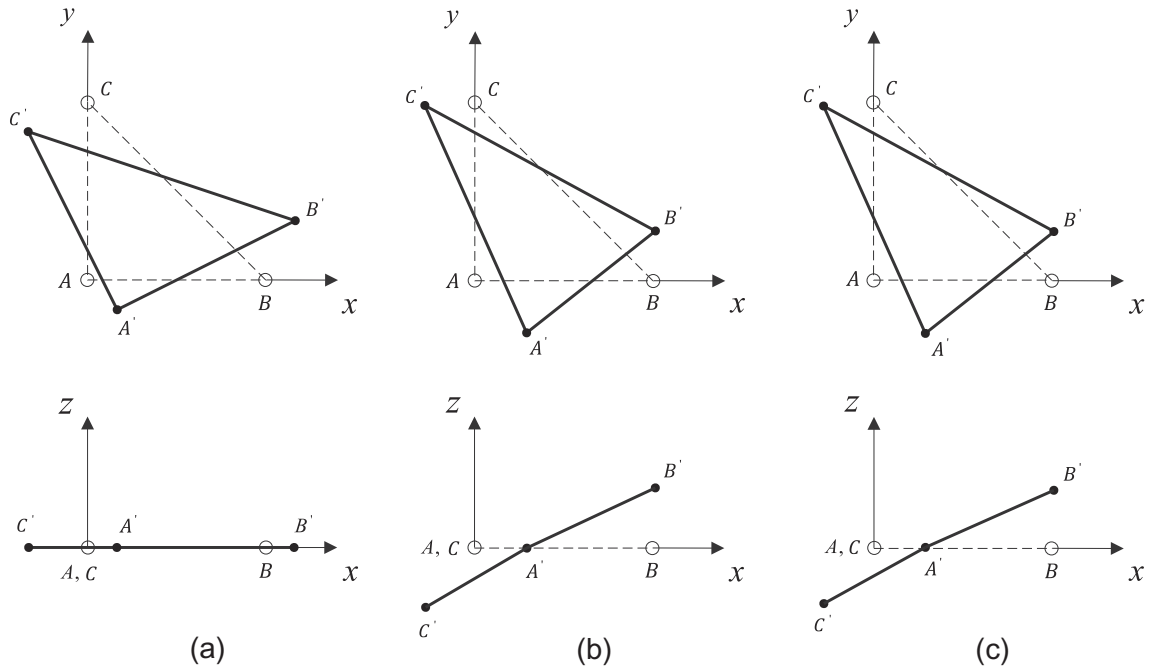

Fig. 5. Shapes of the normalized 10th strain energy mode. The dotted and solid lines correspond to the top surfaces before and after deformation, respectively. (a) Displacement based 3-node shell finite element. (b) MITC3 shell finite element (MITC3-HR shell finite element when $\theta = 0$ deg). (c) MITC3-HR shell finite element when $\theta = 89$ deg.

and MITC3-HR shell finite elements includes a bending mode as well as the pure in-plane twisting mode (Fig. 5(b) and (c)). Also, we note that the 10th mode shape of the MITC3-HR shell finite elements varies depending on the angle θ, but the change is very small, see Fig. 5(b) and (c).

We then investigate how the strain energy of the MITC3-HR shell finite element varies according to the rotation angle (θ) of the contravariant base vector in the in-plane twisting mode. Note that the in-plane twisting mode results in only non-zero transverse shear strains. When the single triangular elements shown in Fig. 4(a) are twisted at the angle φ about the z-axis located at the barycenter, the in-plane twisting mode shown in Fig. 4(b) is obtained: $\theta_x^A = \theta_x^C = \theta_y^A = \theta_y^B = 1/\sqrt{12}$, $\theta_x^B = \theta_y^C = -2/\sqrt{12}$. The single displacement based 3-node and MITC3 shell finite elements give the exact strain energy in the in-plane twisting mode, which results in only non-zero transverse shear strains.

Fig. 6 shows the ratio of the strain energy of the MITC3-HR shell finite element to the strain energy of the MITC3 shell finite element depending on the rotation angle of the contravariant base vector ($0 \leqslant \theta \leqslant 89$ deg) when the in-plane twisting mode is applied. Note that less strain energy stored in the element means that the element is more flexible. The MITC3-HR shell finite element has the same flexibility as the MITC3 shell finite element when the rotation angle $\theta = 0$ deg. However, as the angle increases, the MITC3-HR shell finite element becomes increasingly flexible. As the angle approaches 90 deg, the MITC3-HR shell finite element becomes rapidly flexible and the zero strain energy is calculated when $\theta = 90$ deg. Therefore, it can be expected that the 10th mode of the MITC3-HR shell finite element with $\theta = 89$ deg becomes the spurious in-plane twisting mode when $\theta = 90$ deg.

In order to understand why the behaviors of the MITC3-HR shell finite element with $\theta = 0$ deg are identical to the MITC3 shell finite
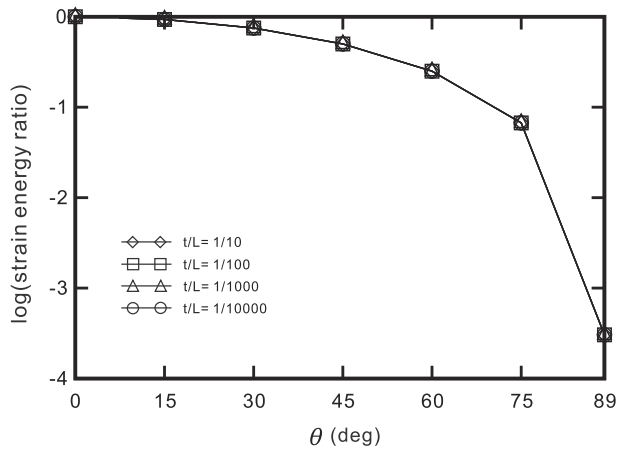
Fig. 6. Ratio of the strain energy of the MITC3-HR shell finite element to the strain energy of the MITC3 shell finite element depending on the rotation angle (θ) of the contravariant base vectors in the in-plane twisting mode.

Fig. 7. A single 3-node triangular shell finite element for the isotropic test. The input values of the geometry are presented in Table 3, $\vec{P} = [F_x \quad F_y \quad F_z \quad M_\alpha \quad M_\beta]^T$.

element and why the MITC3-HR element with θ = 90 deg has a spurious mode, we calculate the approximated transverse shear strains in Eq. (21) for the single triangular element with an uniform thickness (node numbering: 1:A → 2:B → 3:C) in Fig. 4(a) and then separate the covariant transverse shear strain fields corresponding to the original contravariant base vectors $\vec{g}^j$,

$$\bar{e}_{rt}^A = -\alpha_1 \sin\theta + \alpha_2 \cos\theta + \alpha_3(r\sin\theta + s\cos\theta),$$
$$\bar{e}_{st}^A = \alpha_1 \cos\theta + \alpha_2 \sin\theta + \alpha_3(-r\cos\theta + s\sin\theta). \qquad (30)$$

When θ = 0 deg, Eq. (30) has the same form as Eq. (10), this results in $\vec{\gamma}^A = \vec{\gamma}^M$ in Eq. (19). In this case, the MITC3-HR shell finite element becomes identical to the MITC3 shell finite element. In the case of θ = 90 deg, Eq. (30) is as follows:

$$\bar{e}_{rt}^A = -\alpha_1 + \alpha_3 r,$$
$$\bar{e}_{st}^A = \alpha_2 + \alpha_3 s. \qquad (31)$$

In addition, a comparison of Eqs. (31) and (10) shows that the linear terms in each covariant transverse shear strain component are switched. This results in α_3 = 0; thus, the constant transverse shear strain field is obtained. As pointed out in the literature [18], the 3-node plate/shell finite elements with a constant transverse shear strain field display a spurious zero energy mode.

Through the studies in this section, we can conclude that the special approximated transverse shear strain field introduced by the modified Hellinger–Reissner functional selectively increases the flexibility of the MITC3 shell finite element corresponding to the 10th strain energy mode. In other words, the transverse shear strains by the 10th strain energy mode that contains both the in-plane twisting and bending modes becomes smaller in the MITC3-HR shell finite element.

In all the following numerical examples, we use the rotation angle of the contravariant base vectors, θ = 89 deg, to make the MITC3-HR shell finite element flexible enough in the 10th strain energy mode without the spurious energy mode.
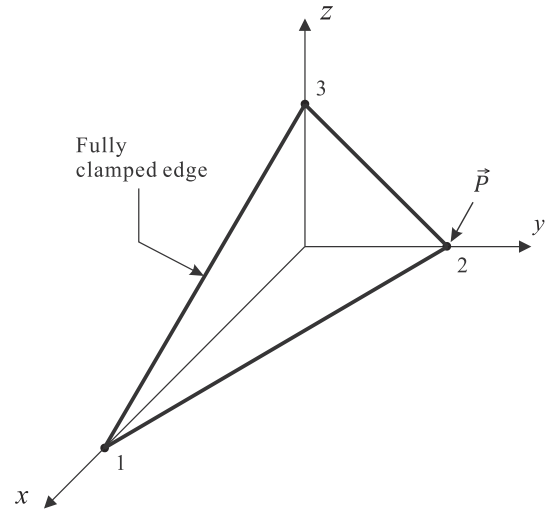
5.2. Isotropic element test

A single 3-node triangular shell finite element in Fig. 7 is analyzed with three different node numberings. All the input values are the same except for the node numbering. Different sequences of node numberings are used as follows: 1 → 2 → 3, 2 → 3 → 1, and 3 → 1 → 2. The results should be the same for all possible tip forces and moments. The input values of the geometry of the 3-node triangular shell element are presented in Table 3. Each node has different thickness and director vectors, which are not normal to the shell midsurface in order to consider a general case.

The MITC3-HR shell finite element gives identical results regardless of the numbering sequences; that is, the element passes the isotropic element test as the MITC3 shell finite element does. Also, the isotropic behavior is independent of the rotation angle of the contravariant base vectors. Of course, the MITC3-HR element shows isotropic behavior for other arbitrary element geometries.

5.3. Patch test

We use the mesh shown in Fig. 8 to perform the patch test [1]. The minimum number of degrees of freedom is constrained so as to prevent rigid body motions. Nodal forces that should result in constant stress conditions are applied. The constant stress should be calculated to pass the patch test. The MITC3-HR shell finite element passes the membrane, bending, and transverse shearing patch tests.

6. Convergence studies

In this section, well-established convergence studies are performed for the MITC3-HR shell finite element developed in this study and the results are compared with those of the MITC3 shell

Table 3
The input values for the geometry shown in Fig. 7 for the isotropic test.

Node (i)	Cartesian coordinate ($\bar{x}_i$)			Director vectors (V_n^i)			Thicknesses
	x_i	y_i	z_i	V_{nx}^i	V_{yx}^i	V_{nz}^i	
1	2.0	0.0	0.0	0.43775	0.87549	0.20467	0.1
2	0.0	1.0	0.0	−0.18273	0.69520	0.69520	0.01
3	0.0	0.0	1.0	0.43775	0.20467	0.87549	0.2
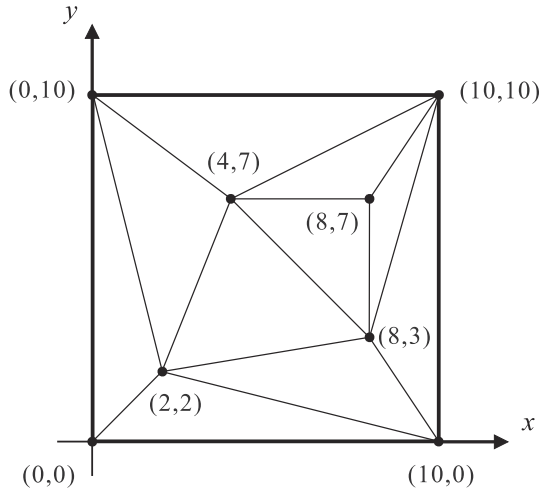
Fig. 8. Triangular mesh used for the patch tests.

$$\vec{\varepsilon} = [\, \varepsilon_{xx} \quad \varepsilon_{yy} \quad \varepsilon_{zz} \quad 2\varepsilon_{xy} \quad 2\varepsilon_{yz} \quad 2\varepsilon_{zx} \,]^{T},$$
$$\vec{\tau} = [\, \tau_{xx} \quad \tau_{yy} \quad \tau_{zz} \quad 2\tau_{xy} \quad 2\tau_{yz} \quad 2\tau_{zx} \,]^{T}, \tag{33}$$

and

$$\Delta\vec{\varepsilon} = \vec{\varepsilon} - \vec{\varepsilon}_h, \quad \Delta\vec{\tau} = \vec{\tau} - \vec{\tau}_h. \tag{34}$$

The position vectors $\vec{x}$ and $\vec{x}_h$ correspond to the continuum domain and the discretized domain, respectively, and the relationship with a one-to-one mapping Π is given as

$$\vec{x} = \Pi(\vec{x}_h). \tag{35}$$

The theoretical convergence behavior can be estimated by

$$\|\vec{u} - \vec{u}_h\|_s^2 \cong ch^k, \tag{36}$$

in which c is a constant and h denotes the element size. When the 3-node shell element is uniformly optimal, the constant is independent of the shell thickness and $k = 2$.

Instead of the exact solution, the finite element solution calculated by a very fine mesh can be practically used,

$$\|\vec{u}_{ref} - \vec{u}_h\|_s^2 = \int_{\Omega_{ref}} \Delta\vec{\varepsilon}^T \Delta\vec{\tau} \, d\Omega_{ref} \tag{37}$$

with

$$\Delta\vec{\varepsilon} = \vec{\varepsilon}_{ref} - \vec{\varepsilon}_h, \quad \Delta\vec{\tau} = \vec{\tau}_{ref} - \vec{\tau}_h, \quad \vec{x}_{ref} = \Pi_{ref}(\vec{x}_h). \tag{38}$$

To measure the convergence of the finite elements in the shell problems with various shell thicknesses, the relative error E_h is used,

$$E_h = \frac{\|\vec{u}_{ref} - \vec{u}_h\|_s^2}{\|\vec{u}_{ref}\|_s^2}. \tag{39}$$

The numerical procedure to calculate the s-norm for shell finite element solutions with general types of elements and general meshes is explained in detail in Ref. [18]. In the use of Eq. (39), it
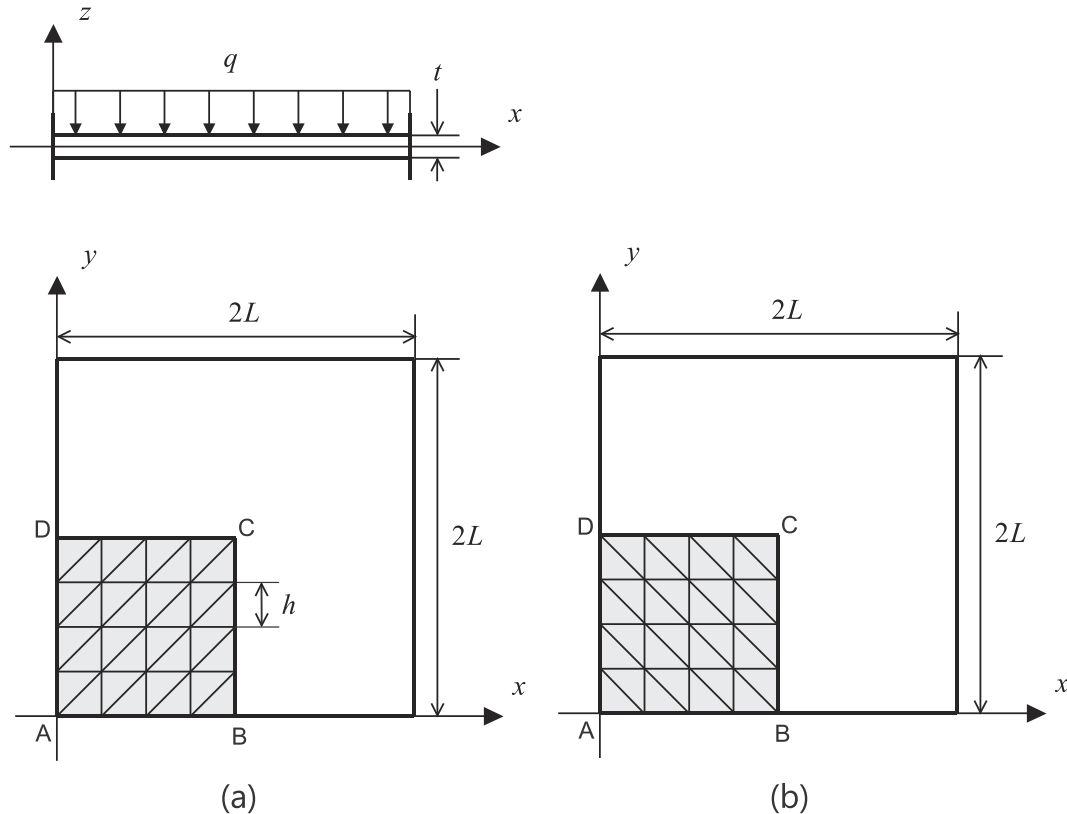
finite element. We consider various shell problems: a clamped plate problem, sixty-degree skew plate problem, cylindrical shell problems, and hyperboloid shell problems [2,15,18,22].

The s-norm proposed by Hiller and Bathe [23] is used to measure the convergence of the finite element solutions. The s-norm is suitable to check whether the finite element solutions satisfy consistency and inf–sup conditions [23–27]. The s-norm is defined as follows

$$\|\vec{u} - \vec{u}_h\|_s^2 = \int_{\Omega} \Delta\vec{\varepsilon}^T \Delta\vec{\tau} \, d\Omega, \tag{32}$$

where $\vec{u}$ is the exact solution, $\vec{u}_h$ is the solution of the finite element discretization, and $\vec{\varepsilon}$ and $\vec{\tau}$ are the strain vector and the stress vector in the global Cartesian coordinate system, respectively, defined by

(a) (b)

Fig. 9. Fully clamped square plate problem under uniform pressure ($L = 1.0$, $E = 1.7472 \times 10^7$, $q = 1.0$ and $v = 0.3$) with two different 4×4 mesh patterns in (a) and (b).
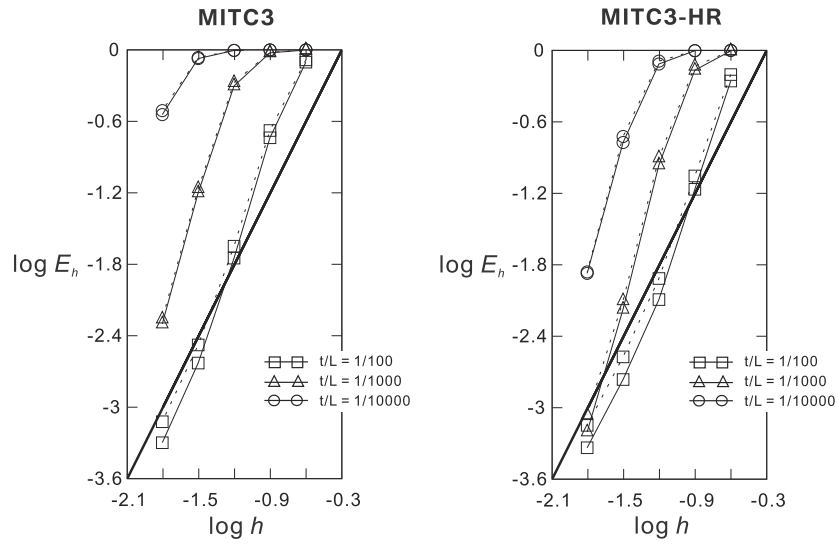
Fig. 10. Convergence curves for the fully clamped square plate problem. The bold line represents the optimal convergence rate. The solid and dotted lines correspond to the results obtained by the mesh patterns in Fig. 9(a) and (b), respectively.
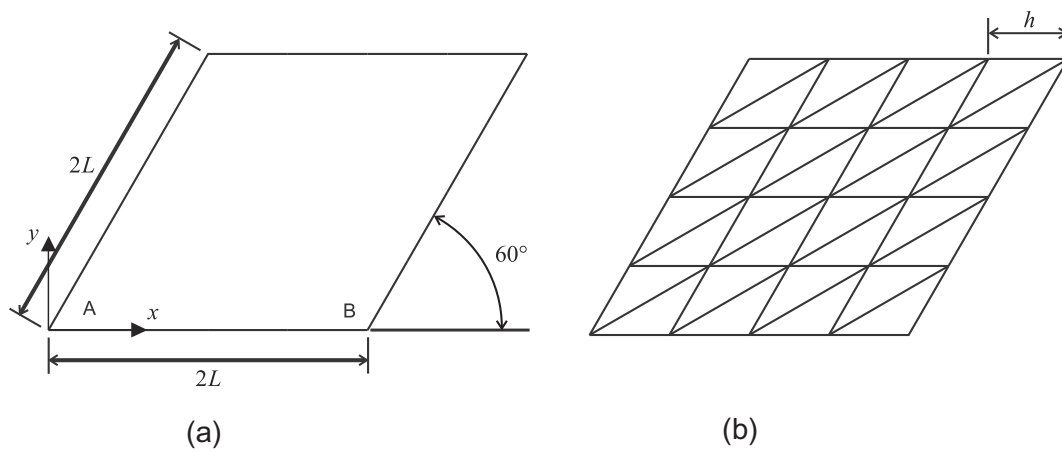

Fig. 11. Simply supported sixty-degree skew plate problem ($L = 1.0$, $E = 1.7472 \times 10^7$ and $v = 0.3$). (a) Problem solved. (b) Mesh pattern used for $N = 4$.
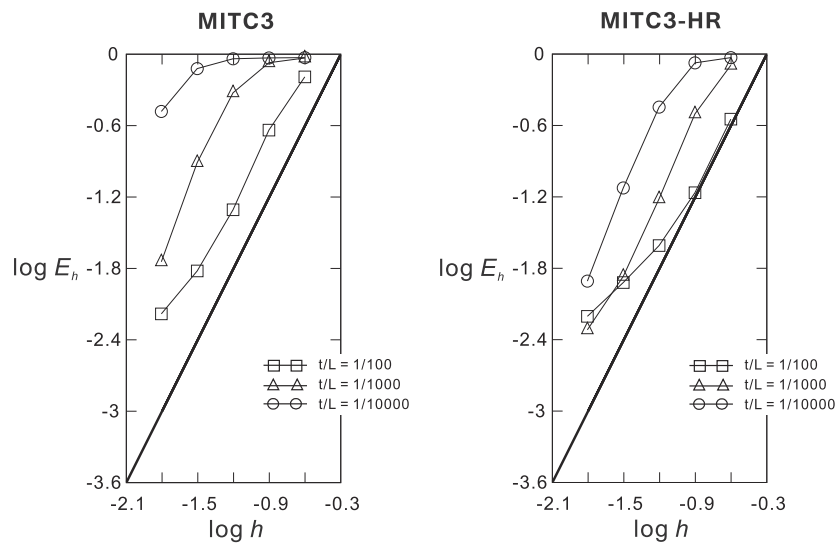

Fig. 12. Convergence curves for the simply supported sixty-degree skew plate problem. The bold line represents the optimal convergence rate.
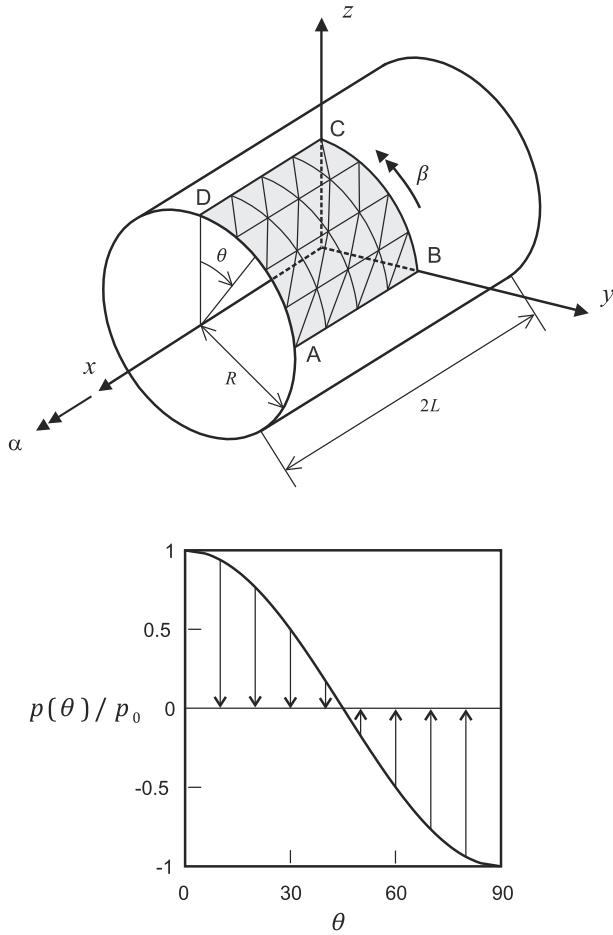
Fig. 13. Cylindrical shell problem (4×4 mesh, $L = R = 1.0$, $E = 2.0 \times 10^5$, $v = 1/3$ and $p_0 = 1.0$).

is very important to use accurate reference solutions calculated by reliable shell finite elements. In this study, we use well-converged reference solutions calculated by fine meshes of MITC9 shell finite elements. Of course, the MITC9 shell finite element is known to satisfy ellipticity and consistency conditions and to show adequate convergences for the shell problems studied in this paper, see Refs. [16,22,23].

In the following sections, we present the convergence curves of the MITC3 and MITC3-HR shell finite elements to show the improved performance of the MITC3-HR shell finite element compared to the MITC3 shell finite element. Note that some of the convergence curves of the MITC3 shell finite element have been published before in Refs. [15,18].

6.1. Fully clamped square plate problem

The plate bending problem shown in Fig. 9 is considered. A square plate of dimensions $2L \times 2L$ with uniform thickness t is subjected to uniform pressure normal to the flat surface and all the edges are fully clamped. Due to symmetry, only a one-quarter model is considered, with the following boundary conditions imposed: $u_x = \theta_y = 0$ along BC, $u_y = \theta_x = 0$ along DC and $u_x = u_y = u_z = \theta_x = \theta_y = 0$ along AB and AD [15,18].

The convergence curves of the MITC3 and MITC3-HR shell elements calculated by Eq. (39) are shown in Fig. 10. The reference solution is obtained by a mesh of 96×96 MITC9 shell finite elements. The solutions of the MITC3 and MITC3-HR shell finite elements are calculated by $N \times N$ meshes ($N = 4, 8, 16, 32,$ and 64). The element size is $h = L/N$. For the range of t/L (1/100, 1/1000, and 1/10,000) considered, the performance of the MITC3-HR shell finite element is much better than that of the MITC3 shell finite element.

6.2. Simply supported sixty-degree skew plate problem

The simply supported skew plate with edges of $2L$ and uniform thickness t is subjected to uniform pressure normal to the flat surface, as shown in Fig. 11. The boundary condition $u_z = 0$ is imposed along all edges [22].

Fig. 12 shows the convergence curves of the MITC3 and MITC3-HR shell finite elements in the simply supported skew plate problem. A mesh of 128×128 MITC9 shell finite elements is used for the calculation of the reference solution. $N \times N$ meshes ($N = 8, 16, 32, 64,$ and 128) are used to evaluate the solutions of the MITC3 and MITC3-HR shell finite elements. The element size is $h = 2L/N$. The graphs indicate the improved capability of the MITC3-HR shell finite element compared with the original MITC3 element.
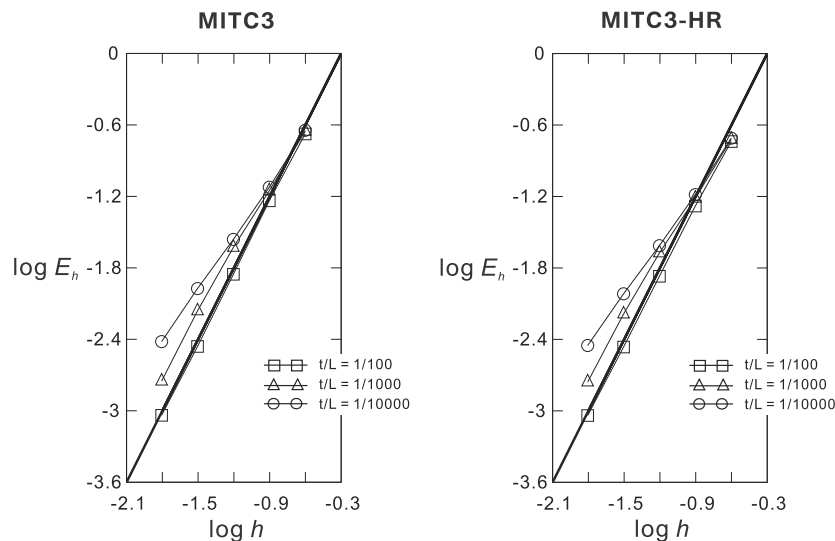

Fig. 14. Convergence curves for the clamped cylindrical shell problem. The bold line represents the optimal convergence rate.
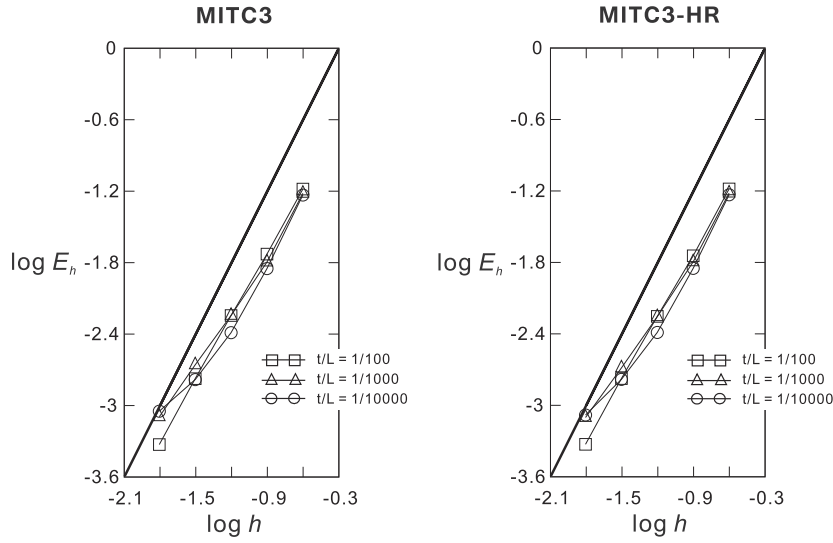
Fig. 15. Convergence curves for the free cylindrical shell problem. The bold line represents the optimal convergence rate.
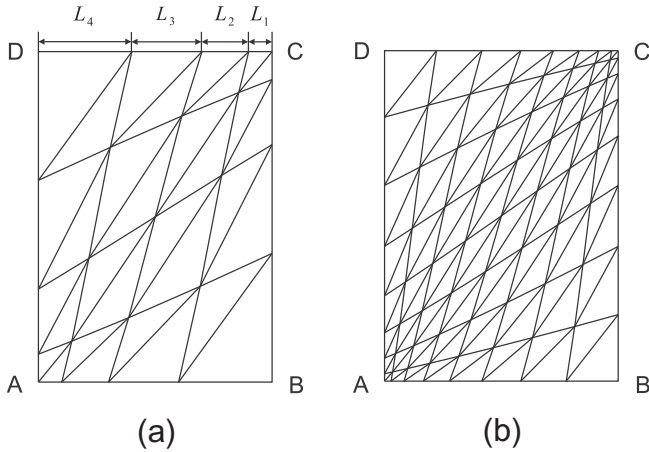

Fig. 16. Distorted meshes for the cylindrical shell problem. (a) Mesh pattern used for N = 4. (b) Mesh pattern used for N = 8.

6.3. Cylindrical shell problems

A cylindrical shell of uniform thickness t, length $2L$, and radius R is considered, as seen in Fig. 13. The loading is smoothly varying periodic pressure $p(\theta)$ normal to the shell surface

$$p(\theta) = p_0 \cos(2\theta). \tag{40}$$

The shell presents two different asymptotic behaviors depending on the boundary conditions at both ends: the bending dominated behavior under a free boundary condition and the membrane dominated behavior under a clamped boundary condition.

Considering the symmetry of the problems, the region ABCD in Fig. 13 is modeled. In the membrane dominated case, the clamped boundary condition is imposed: $u_x = \beta = 0$ along BC, $u_y = \alpha = 0$ along DC $u_z = \alpha = 0$ along AB, and $u_x = u_y = u_z = \alpha = \beta = 0$ along AD. In the bending dominated case, the free boundary condition is imposed: $u_x = \beta = 0$ along BC, $u_y = \alpha = 0$ along DC, and $u_z = \alpha = 0$ along AB [15].
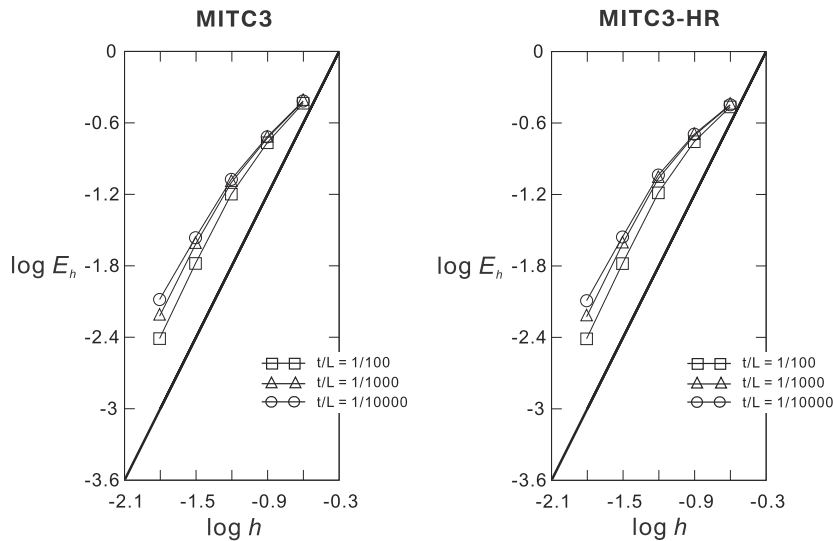

Fig. 17. Convergence curves for the clamped cylindrical shell problem with the distorted meshes shown in Fig. 16. The bold line represents the optimal convergence rate.
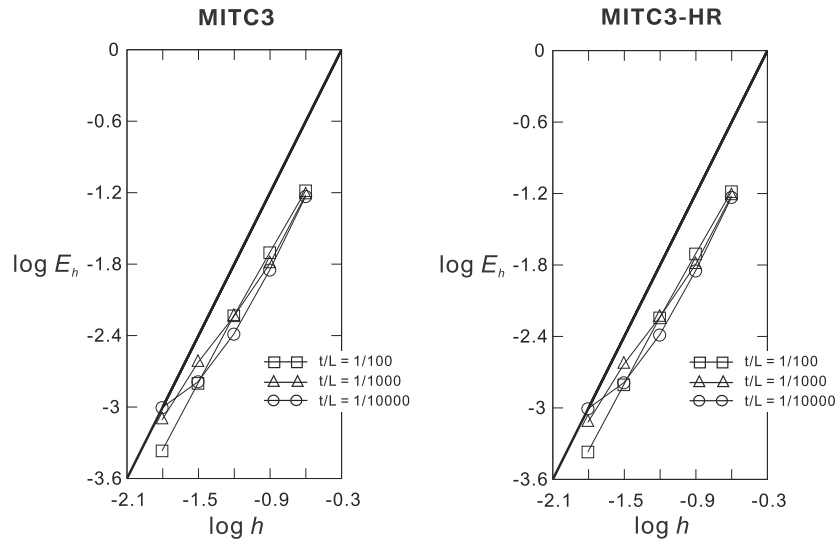
MITC3

MITC3-HR

Fig. 18. Convergence curves for the free cylindrical shell problem with the distorted meshes shown in Fig. 16. The bold line represents the optimal convergence rate.
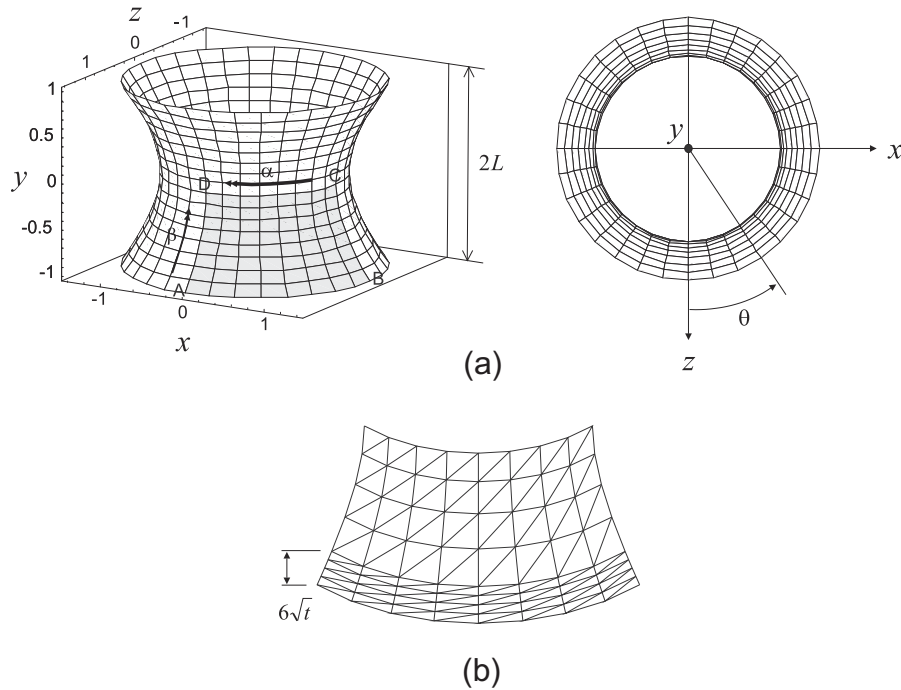

(a)

(b)

Fig. 19. Hyperboloid shell problem ($E = 2.0 \times 10^{11}$, $v = 1/3$ and $p_0 = 1.0$). (a) Problem solved. (b) Graded mesh for the clamped case (8×8 mesh, $t/L = 1/1000$).

Figs. 14 and 15 present the convergence behaviors of the MITC3 and MITC3-HR shell finite elements for the clamped and free cylindrical shell problems, respectively. The reference solution is calculated by a mesh of 96×96 MITC9 shell finite elements for both cases. The solutions of the MITC3 and MITC3-HR shell finite elements are obtained by $N \times N$ meshes ($N = 4, 8, 16, 32,$ and 64). The element size is $h = L/N$. Excellent convergence behavior of the MITC3 element in the cylindrical shell problems has been reported in Ref. [15]. The MITC3-HR shell finite element similarly shows excellent convergence behavior.

It is valuable to study the convergence behaviors of the MITC3 and MITC3-HR shell finite elements for the distorted meshes shown in Fig. 16. When the $N \times N$ mesh is used, each edge is divided by the following ratio: $L_1 : L_2 : \ldots : L_N = 1 : 2 : \ldots : N$. Figs. 17

and 18 present the convergence curves for the clamped and free cylindrical shell problems, respectively. Although the extremely distorted mesh is used, the MITC3 and MITC3-HR shell finite elements still present good convergence behavior.

6.4. Hyperboloid shell problems

The hyperboloid shell is considered as in Fig. 19 and the midsurface of the shell structure is given by

$$x^2 + z^2 = 1 + y^2; \quad y \in [-1, 1]. \tag{41}$$

Smoothly varying periodic pressure normal to the surface is applied,

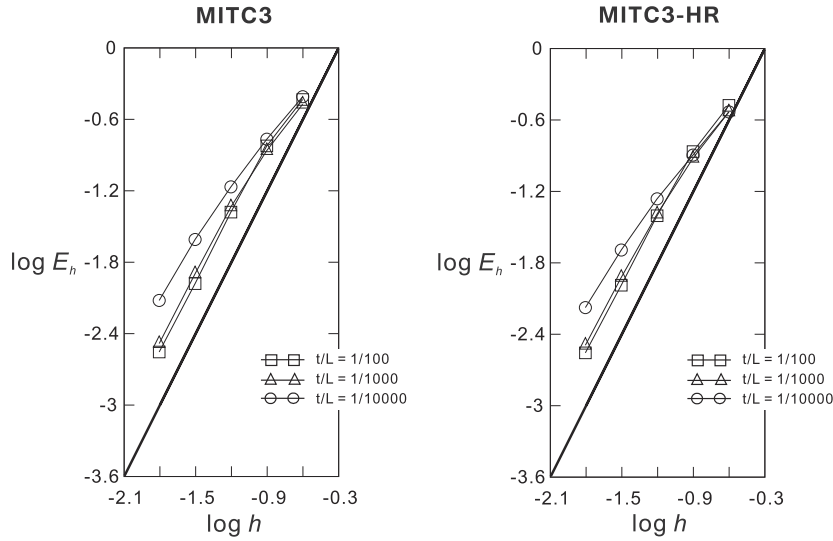$$p(\theta) = p_0 \cos(2\theta), \tag{42}$$

Fig. 20. Convergence curves for the clamped hyperboloid shell problem. The bold line represents the optimal convergence rate.
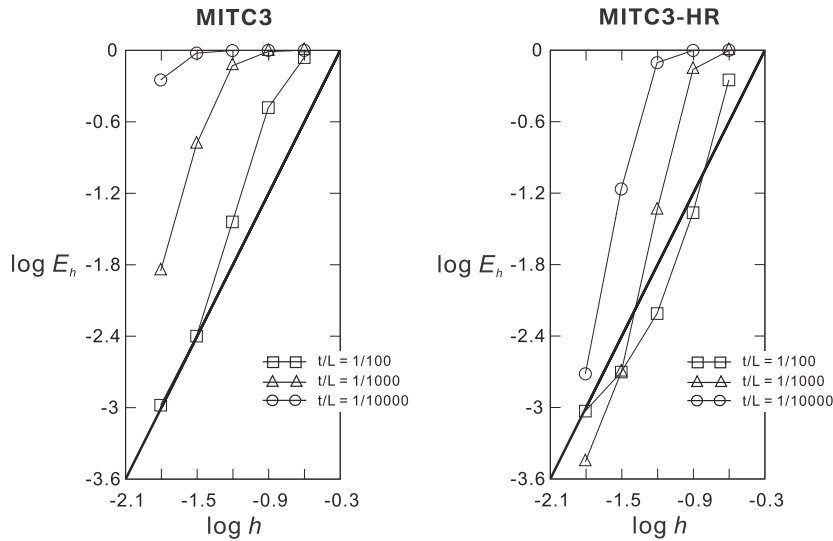

Fig. 21. Convergence curves for the free hyperboloid shell problem. The bold line represents the optimal convergence rate.

which has the same distribution as shown in Fig. 13.

When both ends are clamped, a membrane dominated problem is obtained, and when the ends are free, a bending dominated problem is obtained. The bending dominated hyperboloid shell problem is known to be very difficult to solve [11,15,18].

Due to symmetry, the analyses are carried out in one-eighth of the structure, corresponding with the shaded region ABCD in Fig. 19(a). For the membrane dominated case, the clamped boundary condition is imposed: $u_z = \beta = 0$ along BC, $u_x = \beta = 0$ along AD, and $u_y = \alpha = 0$ along DC, and $u_x = u_y = u_z = \alpha = \beta = 0$ along AB. For the bending dominated case, the free boundary condition is imposed: $u_z = \beta = 0$ along BC, $u_x = \beta = 0$ along AD, and $u_y = \alpha = 0$ along DC [15,18].

In both cases, we use the reference solutions calculated with a mesh of 96×96 MITC9 shell finite elements. The solutions of the MITC3 and MITC3-HR shell finite elements are evaluated by $N \times N$ meshes ($N = 4, 8, 16, 32,$ and 64). The element size is $h = L/N$.

In the clamped hyperboloid shell problem, a boundary layer of width $6\sqrt{t}$ is used for half of the mesh; see Fig. 19(b). In the free hyperboloid shell problem, the thin boundary layer is not specially meshed.

For both the membrane and bending dominated cases, the convergence curves are shown in Figs. 20 and 21. In the membrane dominated case (that is, the clamped hyperboloid shell problem), the performance of the MITC3-HR shell finite element is almost the same as that of the MITC3 shell finite element. Fig. 21 displays the substantially improved performance of the MITC3-HR shell finite element compared to the MITC3 shell finite element.

Finally, Fig. 22 presents the convergence curves of the MITC3-HR shell finite element for the free hyperboloid shell problem depending on the rotation angle (θ) of the contravariant base vectors. As the angle approaches to 90 deg, the performance of the MITC3-HR shell finite element becomes better.

7. Conclusions

The objective of this paper is to improve the MITC3 shell finite element without losing the desirable characteristics of the MITC3 shell finite element. The MITC3-HR shell finite element was developed by using the modified Hellinger–Reissner (HR) functional and applying the rotated approximated transverse shear strain field.
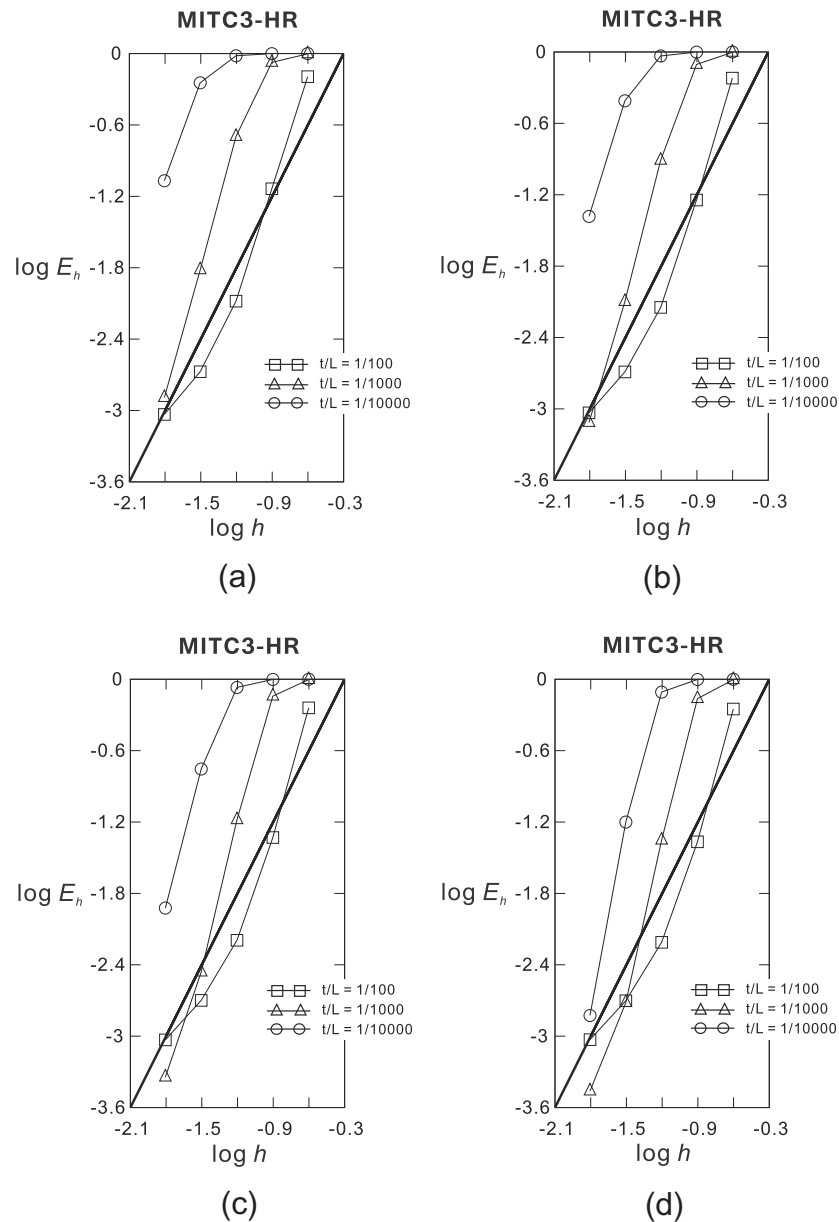
Fig. 22. Convergence curves for the free hyperboloid shell problem depending on the rotation angle (θ) of the contravariant base vectors. The bold line represents the optimal convergence rate. (a) θ = 75 deg, (b) θ = 80 deg, (c) θ = 85 deg, and (d) θ = 90 deg.

The results of the basic numerical tests show that the MITC3-HR shell finite element satisfies all the basic requirements. The results of the convergence studies proved that the MITC3 shell finite element is successfully improved; that is, the MITC3-HR shell finite element shows much better convergence behavior than the MITC3 shell finite element, especially in bending-dominated problems. Interestingly, although the single MITC3-HR shell finite element is very flexible in the in-plane twisting mode, any loss of solution accuracy was not observed in the convergence studies performed in this paper. The MITC3 shell finite element is improved significantly but locking still exists. Hence, further research efforts are required to develop a uniformly optimal 3-node triangular shell finite element.

Acknowledgement

References

[1] Bathe KJ. Finite element procedures. New York: Prentice Hall; 1996.
[2] Chapelle D, Bathe KJ. The finite element analysis of shells-fundamentals. 2nd ed. Berlin: Springer; 2011.
[3] Chapelle D, Bathe KJ. Fundamental considerations for finite element analysis of shell structures. Comput Struct 1998;66:19–36. 711–712.
[4] Lee PS, Bathe KJ. On the asymptotic behavior of shell structures and the evaluation in finite element solutions. Comput Struct 2002;80:235–55.
[5] Baiocchi C, Lovadina C. A shell classification by interpolation. Math Models Meth Appl Sci 2002;12(10):1359–80.
[6] Beirão da Veiga L. Asymptotic energy behavior of two classical intermediate benchmark shell problems. Math Models Meth Appl Sci 2003;13:1279–302.
[7] Beirão da Veiga L. Uniform error estimates for a class of intermediate cylindrical shell problems. Numer Math 2004;96:661–89.
[8] Pitkäranta J, Leino Y, Ovaskainen O, Piila J. Shell deformation states and finite element method: a benchmark study of cylindrical shells. Comput Meth Appl Mech Eng 1995;128:81–121.

[9] Hakula H, Leino Y, Pitkäranta J. Scale resolution, locking, and high-order finite element modeling of shells. Comput Meth Appl Mech Eng 1996;133:157–82.

[10] Bathe KJ, Chapelle D, Lee PS. A shell problem 'highly sensitive' to thickness changes. Int J Numer Meth Eng 2003;57:1039–52.

[11] Lee PS, Bathe KJ. Insight into finite element shell discretizations by use of the "basic shell mathematical model". Comput Struct 2005;83:69–90.

[12] Dvorkin EN, Bathe KJ. A continuum mechanics based four-node shell element for general nonlinear analysis. Eng Comput 1984;1:77–88.

[13] Bathe KJ, Dvorkin EN. A formulation of general shell elements – the use of mixed interpolation of tensorial components. Int J Numer Meth Eng 1986;22:697–722.

[14] Bucalem ML, Bathe KJ. Higher-order MITC general shell elements. Int J Numer Meth Eng 1993;36:3729–54.

[15] Lee PS, Bathe KJ. Development of MITC isotropic triangular shell finite elements. Comput Struct 2004;82:945–62.

[16] Bathe KJ, Lee PS, Hiller JF. Towards improving the MITC9 shell element. Comput Struct 2003;81:477–89.

[17] Beirão da Veiga L, Chapelle D, Paris Suarez I. Towards improving the MITC6 triangular shell element. Comput Struct 2007;85:1589–610.

[18] Lee PS, Noh HC, Bathe KJ. Insight into 3-node triangular shell finite elements: the effects of element isotropy and mesh patterns. Comput Struct 2007;85:404–18.

[19] To CWS, Liu ML. Hybrid strain based three-node flat triangular shell finite elements. Finite Elem Anal Des 1994;17:169–203.

[20] Rhiu JJ, Lee SW. A new efficient mixed formulation for thin shell finite element models. Int J Numer Meth Eng 1987;24:581–604.

[21] Bathe KJ, Iosilevich A, Chapelle D. An evaluation of the MITC shell elements. Comput Struct 2000;75:1–30.

[22] Lee PS, Bathe KJ. The quadratic MITC plate and MITC shell elements in plate bending. Adv Eng Software 2010;41:712–28.

[23] Hiller JF, Bathe KJ. Measuring convergence of mixed finite element discretizations: an application to shell structures. Comput Struct 2003;81:639–54.

[24] Bathe KJ, Iosilevich A, Chapelle D. An inf-sup test for shell finite elements. Comput Struct 2000;75:439–56.

[25] Bathe KJ. The inf-sup condition and its evaluation for mixed finite element methods. Comput Struct 2001;79:243–52. 971.

[26] Bathe KJ, Lee PS. Measuring the convergence behavior of shell analysis schemes. Comput Struct 2011;89:285–301.

[27] Chapelle D, Bathe KJ. The mathematical shell model underlying general shell elements. Int J Numer Meth Eng 2000;48:289–313.